



Higher-order topological insulators by ML-enhanced topology optimization

Zongliang Du^{a,b,*}, Jiachen Luo^a, Zhiang Xu^a, Zhenhao Jiang^c, Xianggui Ding^a, Tianchen Cui^a, Xu Guo^{a,b,**}

^a State Key Laboratory of Structural Analysis, Optimization and CAE Software for Industrial Equipment, Department of Engineering Mechanics, Dalian University of Technology, Dalian, 116023, China

^b Ningbo Institute of Dalian University of Technology, Ningbo, 315016, China

^c School of Data Science, The Chinese University of Hong Kong, Hongkong, 518000, China



ARTICLE INFO

Keywords:

Higher-order topological insulators
Fast design
Topology optimization
Machine learning
Programmable mechanical imaging device

ABSTRACT

Energy in lower dimensions, such as edges or corners, can be robustly confined by the higher-order topological insulators (HOTIs) against defects. Being promising for wave manipulation, the unique property of HOTIs is protected by the associated topological invariant and bulk band. Nevertheless, it is still challenging to fast design topologically nontrivial continuum unit cells with highly localized edge/corner modes in photonic and phononic systems. In the present work, with the help of a multitask learning model simultaneously predicting the discrete-valued topological invariant and continuum-valued bandgap range, a fast design framework is developed using an explicit topology optimization method for mechanical HOTIs. In the solution process, the machine learning model and backpropagation algorithm are integrated into a MultiStart solver to accelerate the design efficiency by 3–4 orders than the traditional topology optimization method. Furthermore, a novel programmable mechanical imaging device illustrates the applications of the optimized HOTI with highly localized corner states. This AI-enhanced design paradigm can be easily extended for the fast design of optimized topological materials among various physical systems.

1. Introduction

Protected by the quantized topological invariants, topological insulators (TIs) supply robust edge or surface states against disorder and defects [1,2]. A system is named a higher-order topological insulator (HOTI) as it insulates in bulk and only supports protected gapless modes at its boundaries of higher codimensions, e.g., the corners of a 2D material [3,4]. In photonic and phononic systems, the macroscopic continuum unit cells offer a full degree of freedom to manifest the topological effect, and exploring HOTIs has attracted an ever-increasing interest [5–19], for their scientific significance and potential applications. Therefore, a fast and systematic design paradigm for HOTIs in photonic and phononic systems is highly desired.

Besides the well-developed discrete models of topological insulators, e.g., the spring-mass systems [20–23], rods and beams [24–27], the continuum models offer a larger degree of design freedom yet are more difficult to be created by designers. Recently, topology optimization has been successfully applied to the systematic design of topological insulators. By realizing the novel wave propagation path in a well-designed waveguide, acoustic and photonic spin-Hall insulators are

obtained through topology optimization [28,29]. Band structures with Dirac cones are rationally obtained by topology optimization, and nontrivial bandgaps of spin-Hall insulators are produced by breaking the symmetry of the obtained C_3 - and C_6 -symmetric hexagonal unit cells [30,31]. Through customizing specific degeneracies in the spin-Hall effect, novel broadband phononic topological insulators in C_2 - and C_4 -symmetric square lattices are obtained and enlarge the set of phononic topological materials [32,33]. In [34], describing the hexagonal unit cells using explicit topology optimization method, a pair of optimized mechanical valley Hall insulators are obtained by constraining the band inversion index and maximizing the operational bandwidth of the supercell. Such band inversion index and topology optimization formulation have been used recently to design square valley Hall insulators [35]. Besides, the idea of maximizing the operational bandwidth of supercell is successfully applied to design ultra-broadband and highly localized energy transport protected by the valley-Hall effect [36]. Recently, as an extension of the design method in [34], a unified and rational design approach applicable to quantum valley/spin-Hall insulators has been developed [37]. Due to the increased difficulties, fewer

* Corresponding author at: State Key Laboratory of Structural Analysis, Optimization and CAE Software for Industrial Equipment, Department of Engineering Mechanics, Dalian University of Technology, Dalian, 116023, China.

** Corresponding author.

E-mail addresses: zldu@dlut.edu.cn (Z. Du), guoxu@dlut.edu.cn (X. Guo).

investigations are reported on the rational design of higher-order topological insulators. In [38], by maximizing the width of the overlapped band gap of the nontrivial and trivial spin-Hall insulators, higher-order photonic topological insulators are produced with the corresponding bulk polarization validated. Later on, this idea is extended by the authors to design photonic and phononic HOTIs with different symmetries induced by the spin-Hall effect and valley-Hall effect [39–41]. By obtaining unit cells with prescribed degeneracies using topology optimization, switchable higher-order topological states are realized based on square unit cells [42]. A recent review reports the development of photonic and phononic TIs employing inverse design methods, including one-dimensional TIs, TIs based on the quantum spin Hall effect and quantum valley Hall effect, and HOTIs in lattices with diverse symmetries [43].

It should be noted that, in most of the above inverse design works, the related topological invariants, which are the essential characteristic of topological insulators, are not involved directly in the optimization formulation but only validated for the optimized design to escape from the computational complexity. To mathematically guarantee the non-trivial topological property in the design process, Luo et al. suggested adding the requirement of topological invariant as a constraint [44]. Instead of dealing with the computationally demanding Berry curvature-related classical topological invariants, symmetry indicators and bulk polarization are used to identify the first- and second-order nontrivial topological crystalline insulators (TCIs) in the 2D point groups [44]. Although the number of design variables of optimized unit cells and the cost of calculating the topological invariants are significantly reduced, using a genetic algorithm (GA), hundreds to thousands of times of evaluation of the topological properties are still time-consuming [44]. Recently, machine learning techniques have been adopted to investigate the topological effect and design TIs; however, many of them are limited to the discrete-type unit cells to keep the number of design variables minimal yet restrict the design space inevitably [45–49]. For phononic systems, topological metaplates and beams with nontrivial topological properties have been obtained by machine learning [50–52]. For the optimal design of mechanical topological waveguide, regression and classification neural networks are trained respectively to predict the ranges of target bandgap and vortex indices to efficiently obtain a pair of valley Hall insulators [53]. Nevertheless, improvements in the neural network models and classification of topological materials can be further investigated in that work.

In the present work, C_{4v} -symmetric continuum unit cells are first described by the explicit topology optimization method to formulate the mathematical programming of designing higher-order mechanical topological insulators. Setting the geometry parameters as the input, a multitask learning model is trained to simultaneously predict their topological labels with discrete values and the ranges of the (nontrivial) bandgaps with continuum values. Incorporating this model and the backpropagation algorithm, optimal HOTIs with highly localized topological corner states can be obtained in about 45 seconds on a desktop computer under the topology optimization framework, roughly 3–4 orders of magnitude in the improvement of efficiency.

The rest of the paper is organized as follows: in Section 2, by describing the C_{4v} -symmetric continuum unit cells using the Moving Morphable Component method and labeling them with the bulk polarization and the range of target bandgap, design formulation is proposed for mechanical HOTIs. To accelerate the solution process, a multitask learning model is constructed to simultaneously predict those discrete-valued and continuum-valued labels simultaneously in Section 3. Incorporating the multitask learning model, Section 4 proposes an ML-enhanced fast design algorithm to produce optimal HOTIs with highly localized corner states. Finally, some concluding remarks are presented in Section 5.

2. Design formulation of mechanical HOTIs using the Moving Morphable Component (MMC) method

Topology optimization aims to distribute available materials in the design domain to achieve optimal performance through solving mathematical programming [54]. Compared to the trial-and-error method, optimized designs with superior performance can be obtained through a rational design process using topology optimization. This section adopts the MMC method to describe the continuum unit cells with explicit geometry parameters. Then the analysis of bulk polarization and normalized band structures is briefly introduced to qualitatively and quantitatively distinguish mechanical HOTIs. Based on that, a topology optimization formulation is developed for optimal mechanical HOTIs. As an alternative to finite element analysis, neural network models can be used to establish a mapping from the geometry to the concerned physical properties of the unit cells.

2.1. Geometry description of continuum unit cells using MMCs - Input

The unit cells are supposed to be square with a side length of 1 m and composed of epoxy resin (base medium, $E_0 = 4.35 \text{ GPa}$, $\nu_0 = 0.37$, $\rho_0 = 1180 \text{ kg/m}^3$) and iron (scatter, $E_1 = 200 \text{ GPa}$, $\nu_1 = 0.3$, $\rho_1 = 7800 \text{ kg/m}^3$). As illustrated in Fig. 1(a), the scatters are described by the so-called Moving Morphable Components (MMCs), which could move, deform and merge through updating their geometry parameters [55–58].

Cubic splines are used to interpolate the boundary of the scatter. For C_{4v} -symmetric unit cells, fixing the scatter at the center, the primitive 1/8 part is determined by the three control points illustrated in Figs. 1(a) and 1(b). In other words, the vector of the radii of the three control points, i.e., $\mathbf{r} = (r_1, r_2, r_3)^\top$, is able to describe the scatter and set as the input of the neural network. Furthermore, as shown in Fig. 1(b), 22 refined interpolation points are introduced and the expanded radii vector $\mathbf{R} = (R_1, \dots, R_{22})^\top$ can be used as an alternative input of the neural network model.

2.2. Identification of HOTIs using the bulk polarization and target bandgap - Output

For C_{4v} -symmetric mechanical unit cells, according to the Floquet-Bloch theorem, the out-of-plane harmonic displacement field u_z can be determined by the following equations:

$$\begin{cases} \mu \left(\frac{\partial^2 u_z}{\partial x^2} + \frac{\partial^2 u_z}{\partial y^2} \right) = -\omega^2 \rho u_z \\ u_z(\mathbf{r} + \mathbf{R}) = e^{i\mathbf{k} \cdot \mathbf{R}} u_z(\mathbf{r}) \end{cases} \quad (1)$$

where μ , ω and ρ are the shear modulus, the angular frequency and the density; \mathbf{k} and \mathbf{R} are the wavevector and the lattice vector, respectively. By taking advantage of the explicit description of the MMC method, the exact geometry model of the unit cells can be constructed parametrically and discretized by body-fitted mesh in COMSOL Multiphysics 5.4 (abbr. COMSOL). Solving Eq. (1) for the wavevector along the boundary of the first irreducible Brillouin zone illustrated by Fig. 1(c), the normalized band structure can be obtained as Fig. 1(d).

The topological corner states always appear in the nontrivial bandgap, and with the same central frequency, a wider bandgap would bring up more localized higher-order edge/corner states. Therefore, the range of the target bandgap is set as part of the labels. In particular, for the n th order bandgap, its normalized lower and upper bounds are saved in pairs as

$$(\bar{\omega}_1, \bar{\omega}_2) = \left(\max_k \omega_n, \min_k \omega_{n+1} \right) \times \frac{A}{2\pi\sqrt{\mu_0/\rho_0}} \quad (2)$$

where $A = 1 \text{ m}$ is the lattice constant.

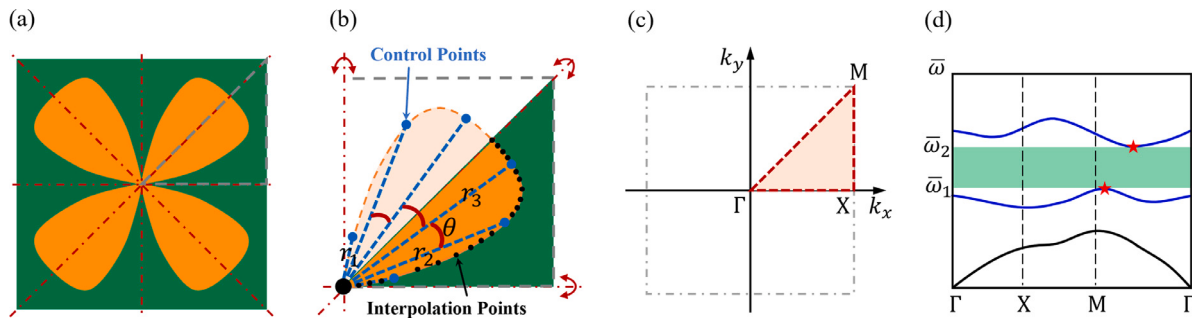


Fig. 1. (a) A C_{4v} -symmetric unit cell described by the MMC method (green: epoxy resin; orange: iron); (b) the 3 control points and the 22 refined interpolation points in the 1/8 unit cell with $\theta = \pi/12$; (c) the first irreducible Brillouin zone of a C_{4v} -symmetric unit cell and (d) the corresponding normalized band structure with stars identifying the range of concerned bandgap.

TCIs are a particular class of topological materials with their topological property protected by the crystallographic symmetry of lattice [59–61]. Luckily, as an effective topological invariant, the bulk polarizations of TCIs can be efficiently calculated based on the symmetry indicators (SIs), which actually reflect the symmetry properties (or the parity) of the eigenmodes at the high symmetry points. The SI method has been successfully applied to discover thousands of new topological materials in the field of physics [62–66].

In particular, the second-order bandgap is fixed as the target for the present C_{4v} -symmetric unit cells. The SIs of the m th band at the high-symmetry points, i.e., ξ^m , can be solved by the following eigenvalue problem

$$\hat{C}_2 |\mathbf{u}_z^m(\mathbf{k}_{sp})\rangle = \xi^m |\mathbf{u}_z^m(\mathbf{k}_{sp})\rangle, \quad \mathbf{k}_{sp} = \mathbf{k}_\Gamma, \mathbf{k}_X \quad (3)$$

where \hat{C}_2 is the symmetry operator of the two high-symmetry points. And the bulk polarization is (P, P) with

$$e^{i2\pi P} = \prod_{m=1,2} \delta^m = \frac{\xi_X^1 \xi_X^2}{\xi_\Gamma^1 \xi_\Gamma^2} \quad (4)$$

For nontrivial unit cells, $P = 1/2$ and topological corner states locate in the range of the second bandgap. Otherwise, zero-valued P implies a trivial topology. Based on the bulk polarization, a binary value T is set for the topological label of each unit cell.

2.3. Topology optimization formulation of optimal mechanical HOTIs

The mathematical programming of designing a mechanical HOTI with a target width $\bar{\omega}_{tar}$ of the normalized bandgap, (i.e., $\text{sgn}(P) = 1$ for the nontrivial topological property and $\bar{\omega}_2 - \bar{\omega}_1 = \bar{\omega}_{tar}$ for the target width requirement), can be formulated as

$$\begin{aligned} \text{find } & \mathbf{r} = (r_1, r_2, r_3)^T \\ \text{min } & f = -\text{sgn}(P) + (\bar{\omega}_2 - \bar{\omega}_1 - \bar{\omega}_{tar})^2 \\ \text{s.t. } & 0.01 \text{ m} \leq r_i \leq 1 \text{ m}, i = 1, 2, 3 \end{aligned} \quad (5)$$

To obtain the optimal HOTIs with highly localized corner states, (i.e., $\text{sgn}(P) = 1$ for the nontrivial topological property and maximized value of $\bar{\omega}_2 - \bar{\omega}_1$ for producing highly localized corner states), the objective function can be modified as¹

$$f = -\text{sgn}(P) + \bar{\omega}_1 - \bar{\omega}_2 \quad (6)$$

In Eqs. (5) and (6), the normalized upper and lower bounds of the target bandgap and the bulk polarization are calculated by Eqs. (1)–(4) through finite element method. At this circumstance, it would be difficult to obtain analytical sensitivities, and the above design formulations could be solved with the help of gradient-free algorithms,

¹ A more rigorous objective function for the most highly localized corner states should be $f = -\text{sgn}(P) + 2(\bar{\omega}_1 - \bar{\omega}_2) / (\bar{\omega}_1 + \bar{\omega}_2)$ to consider the influence of frequency regime.

which usually require hundreds to thousands of times of evaluation of the objective function values [44]. This would be very time-consuming and inspires us to train a machine-learning model for the fast prediction of the desired properties from the MMC parameters.

3. A multitask learning model for the mechanical HOTIs

In this section, the preparation of the dataset is introduced first. Then the structure and the effectiveness of a multitask learning model simultaneously predicting the discretized-valued topological property and continuum-valued bandgap information are sketched.

3.1. Preparation of the dataset

Due to the symmetry, the MMC-described unit cell in Fig. 1(a) is solely determined by its three design variables. To include more sufficient information improving the prediction accuracy², the expanded vector including the radii of the 22 refined interpolation points illustrated by Fig. 1(b), i.e., $\mathbf{X} = (R_1, R_2, \dots, R_{22})^T$, is set as the input.

The output vector includes two groups, i.e., the upper bound, the lower bound and the width of the normalized target bandgap³; and the topological label $T = 1$ or 0 based on the higher-order topological property. Therefore, the output vector denotes $\mathbf{Y} = (\bar{\omega}_1, \bar{\omega}_2, \bar{\omega}_2 - \bar{\omega}_1, T)^T$.

By generating 20,000 groups of control points randomly distributing the r_i ($i = 1, 2, 3$) between its lower and upper bounds, the corresponding inputs and the outputs are obtained using our in-house code with COMSOL. Normalization and data cleaning are adopted for the entire dataset to improve the training efficiency and prediction accuracy. The dataset is shuffled and divided into the training, validation, and test sets by the ratio of 8:1:1.

3.2. A multitask learning model simultaneously predicting the topological property and nontrivial bandgap information

3.2.1. The multitask learning neural network model

In the output vector, the topological label is a binary value and can be predicted by the classification model, while the three variables about bandgap information are continuum valued and should be generally predicted by the regression model. Actually, the joint learning of separate regression and classification tasks form a multitask learning problem [67,68]. This involves simultaneously handling two types of loss functions for both regression and classification problems, and while it is difficult for conventional neural networks.

² The comparison between the prediction accuracy of deep learning models with 3 and 22 input variables is presented in Appendix A.

³ Although the bandgap width is dependent on the upper and lower bounds, as shown in Appendix A, setting $\bar{\omega}_2 - \bar{\omega}_1$ as an independent output variable could improve the prediction accuracy of $\bar{\omega}_1$ and $\bar{\omega}_2$ as well.

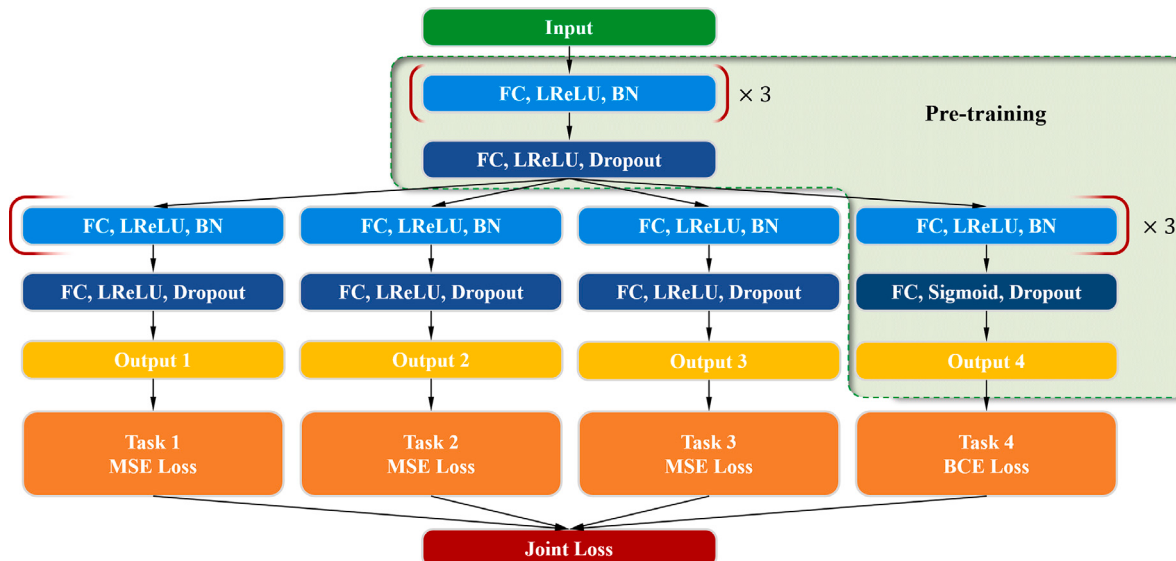


Fig. 2. The MTL neural network model simultaneously predicts the topological property and nontrivial bandgap information of the C_{4v} -symmetric unit cell in Fig. 1. The FC, LReLU, BN, MSE and BCE are the abbreviations of fully connected layers, Leaky Relu activation function, batch normalization, mean square error and binary cross entropy, respectively.

The multitask learning (MTL) neural network model is illustrated in Fig. 2. In the MTL model, the mean-square-error is used to measure the loss of the three regression tasks described as:

$$\text{MSELoss}_k = \frac{1}{N} \sum_{i=1}^N (\hat{Y}_k - Y_k)^2, \quad k = 1, 2, 3 \quad (7)$$

where \hat{Y}_k and Y_k are the actual and the predicted k th output, and N is the batch size. For the classification task, the binary cross entropy is used as the loss function:

$$\text{BCELoss} = -\frac{1}{NM} \sum_{i=1}^N \sum_{j=1}^M w_j (\hat{t}_{ij} \log t_{ij} + (1 - \hat{t}_{ij}) \log (1 - Y_{ij})) \quad (8)$$

where N is the batch size, $M = 2$ is the number of topological label categories, and w_j is the weight of the j th category. The symbols \hat{t}_{ij} and t_{ij} are the actual and predicted probability of the topological label of the i th sample belonging to the j th category.

Since the MTL neural network uses a joint loss function, the model's performance is highly dependent on an appropriate choice of the loss weights for each task. We adopt the homoscedastic task uncertainty as a basis to balance various regression and classification losses automatically [69]. This yields superior performance for the MTL model compared to those that use a naive weighted sum of losses. Specifically, the joint loss is given as:

$$\text{JointLoss} = \frac{1}{\sigma_4^2} \text{BCELoss} + \log \sigma_4 + \sum_{k=1}^3 \left(\frac{1}{\sigma_k^2} \text{MSELoss}_k + \log \sigma_k \right) \quad (9)$$

where σ_k are the corresponding observation noise scalar ($k = 1, 2, 3$ for the regression tasks and $k = 4$ for the classification task).

In the MTL model, a hard parameter-sharing treatment is adopted. Specifically, as shown in Fig. 2, the lower layers are shared across all tasks and are called shared layers; while the top layers are specialized for each task and are called task-specific layers [67]. For the shared layers, four fully connected layers are used to connect the input and task-specific layers, with the number of neurons being 32, 64, 128, and 256 in order. For the task-specific layers, four fully connected layers are used to connect the shared layers and the outputs of the respective tasks, with the number of neurons being 128, 64, 32, and 16 in order. Additionally, the Leaky Relu activation function is used for each hidden layer to introduce nonlinear factors into the neural network. In particular, the output layer uses a Sigmoid activation function to extract the classification probabilities for the classification task. Besides, the

Table 1

Comparison of the prediction accuracies of the MTL model on the validation dataset and the test dataset.

	Validation dataset	Test dataset
Joint loss	-7.446	-7.446
Relative error of the lower bounds	1.71%	1.65%
Relative error of the upper bounds	1.46%	1.37%
Absolute error of the bandwidth	0.0144	0.0141
Classification accuracy of the topological label	98.29%	98.10%

batch normalization method over a 1D input and dropout is added after each activation function to further speed up training and regularize the model [70,71].

3.2.2. Training of the MTL model

The k -fold cross-validation ($k = 9$ in the present work) is adopted to train the model better and evaluate its performance on the entire dataset. In addition, all the hidden layers for the classification task, boxed with dotted lines in Fig. 2, are pre-trained to improve the prediction accuracy. The minibatch size and the max epoch number are set to 500 and 400, respectively. Due to the adoption of early stopping, the actual converged epoch number is generally smaller than 400. As an improvement of the Adam algorithm, the AdamW algorithm [72], is used to accelerate the learning process with an initial learning rate of $\alpha = 0.01$, which is specially updated to half of the previous value when variations of the joint loss of last ten epochs remain no greater than a threshold, e.g., 0.001.

The convergence histories of the joint loss on the training and validation sets are shown in Fig. 3. The quantitative performance of the well-trained MTL model on the validation and test sets are shown in Table 1, which reveals the reliability of the neural network model. Furthermore, the prediction performance of the MTL model on the test set is illustrated in Fig. 4. For the three regression tasks, the predicted values are plotted against the actual values in Figs. 4(a)–(c) with all R-square values greater than 0.99. For the classification task, the confusion matrix of the test set is presented in Fig. 4(d). It should be noted that, the incorrect classification cases are always the marginal data. In particular, for the wrongly classified samples, their predicted and the actual average values of $|\bar{\omega}_1 - \bar{\omega}_2|$ are 0.0175 and 0.0183, respectively. As will be shown in the next section, HOTIs with a small width of nontrivial bandgap are not favorable in real applications.

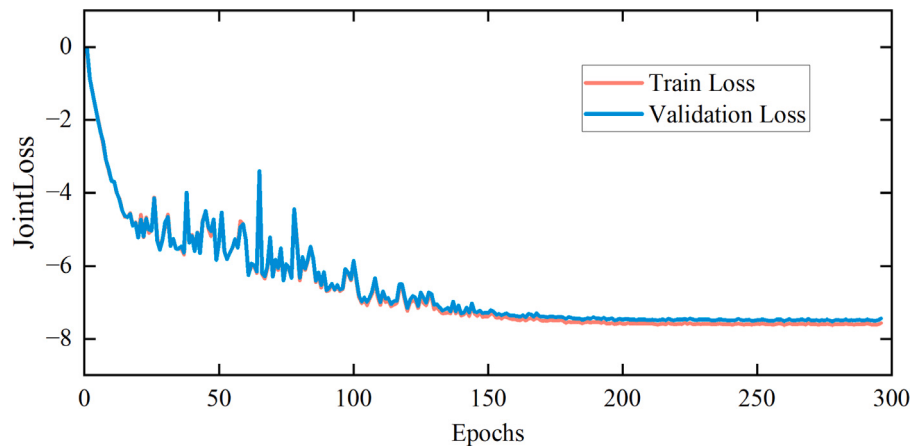


Fig. 3. The iterative history of the joint loss on the training set and validation set of the MTL model.

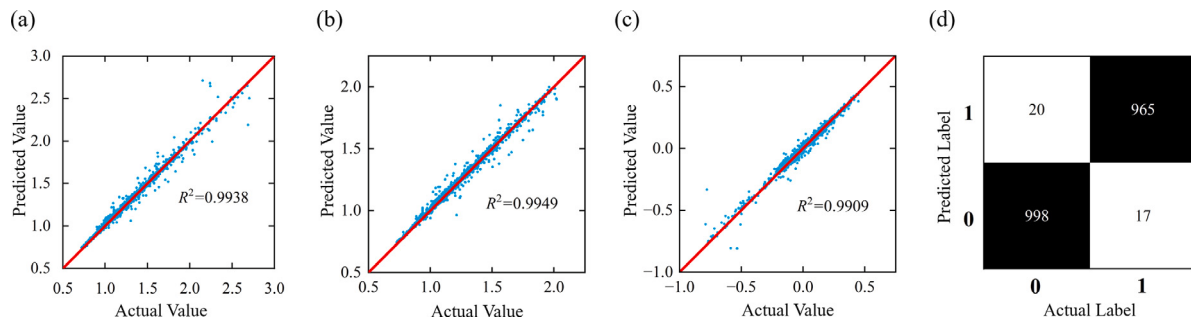


Fig. 4. Illustration of the prediction accuracy of the MTL model on the test set: (a)–(c) the actual and predicted values of the lower bound, the upper bound and the width of the normalized bandgap, respectively; (d) the confusion matrix of the classification task on the topological label.

All those facts demonstrate the effectiveness of the MTL neural network model.

It is worth noting that, the reliable MTL model provides an alternative to the finite element analysis and significantly improves computational efficiency. Analyzing 1, 000 samples, the average time cost for obtaining the output vector is 16.63 s using COMSOL, while it takes only 3.98×10^{-6} s in the MTL model, which is about 4.178×10^6 times more efficient than the former. All calculations are performed using a desktop workstation equipped with an Intel(R) Xeon(R) Gold 6226R CPU @ 2.90 GHz CPU, 512 GB of RAM, NVIDIA GeForce RTX 3090 GPU, Matlab 2022b, COMSOL Multiphysics 5.4, and Pytorch 1.13.0 under Windows Server 2022.

4. Machine learning-enhanced fast design of higher-order topological insulators

With the well-trained machine learning model, the solution process of the topology optimization formulation in Section 2.3 can be greatly improved in efficiency. Using such design formulation, optimized HOTIs with specialized widths and the largest width of nontrivial bandgap are obtained. Furthermore, the significance of the optimized HOTI is validated by its highly localized corner states, and a novel programmable mechanical imaging device illustrates the applications of the optimized HOTI as well.

4.1. The MTL-enhanced solution framework

Besides the significant acceleration for prediction of the topological property and target bandgap information with a high accuracy, the sensitivity information of the design formulation (Eqs. (5) and (6)) can be obtained with the help of the backpropagation of the MTL neural network. In this manner, a gradient-based algorithm, i.e., the

fmincon function in the optimization toolbox of Matlab, can be used to solve the corresponding mathematical programming more efficiently as compared to the gradient-free algorithms in general. Since the gradient-based algorithms could get stuck in local minima, we use the Multistart solver with parallel computing to obtain a best local minima from a number of random starting points as illustrated by Fig. 5.

4.2. Results

4.2.1. Optimized HOTIs with specialized widths of nontrivial bandgap

Setting the width of normalized bandgap as 0.1, 0.15, 0.2, ..., 0.45, Eq. (5) is solved through the MTL-enhanced procedure as Fig. 5 for 100 times, respectively. The average time cost of obtaining the 800 HOTIs is 42.73 s. For all the obtained designs, evaluated by the MTL model, their topological labels are uniformly 1, meanwhile, the relative errors between their expected bandgap widths and the targets are all less than 0.003%. This shows the effectiveness of the backpropagation-based gradient solution procedure with a MultiStart solver. All these optimized designs are analyzed by COMSOL as well. The results reveal that all of the 800 unit cells are actually topologically nontrivial, and the average relative errors of the expected and the actual values of the normalized bandgap width are 5.52%, 5.58%, 2.77%, 1.86%, 2.50%, 2.54%, 2.44% and 1.97% in order. It is reasonable that the relative error of a narrower target bandgap is larger. Some representative histograms of the relative errors of the expected bandgap width are illustrated as Fig. 6 for the cases $\bar{\omega}_{tar} = 0.2, 0.3, 0.4$. All these facts demonstrate the accuracy and confidence of the well-trained MTL model.

Due to the non-convexity of the inverse design problems and the randomness of the starting points in the MultiStart solver⁴, diverse

⁴ The effectiveness of the MultiStart solver is shown in Appendix B.

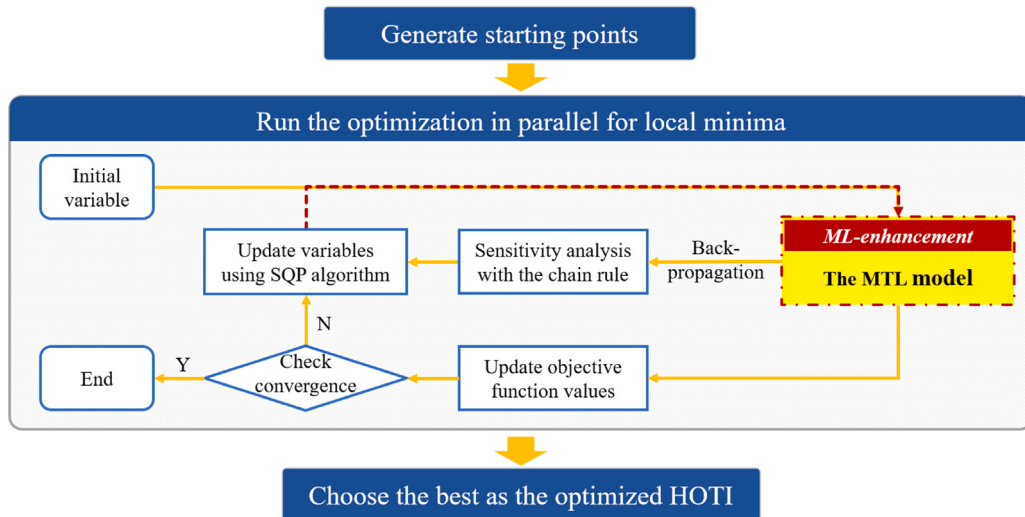


Fig. 5. Flowchart of the MTL-enhanced solution process for fast design of higher-order topological insulators using explicit topology optimization method.

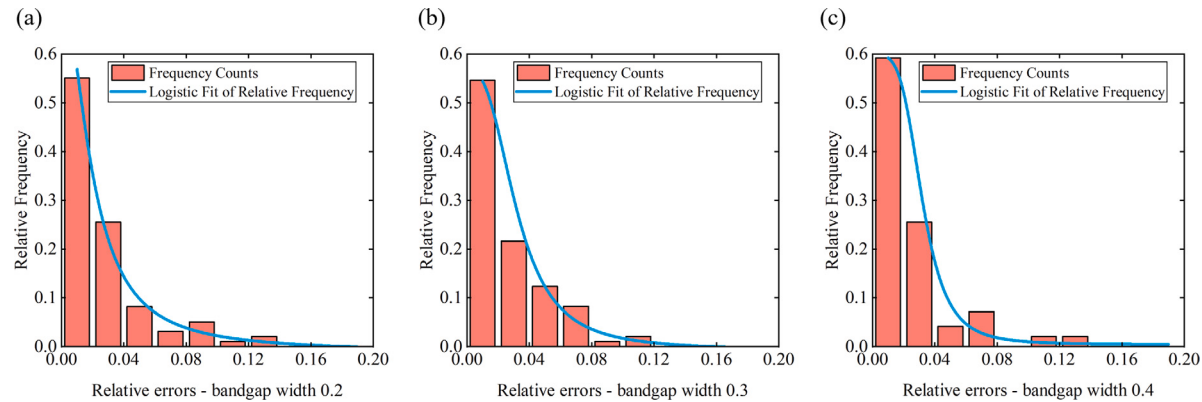


Fig. 6. Histograms of the relative errors of the expected and the actual normalized bandgap width for the target values of (a) 0.2; (b) 0.3 and (c) 0.4, respectively.

design results can be obtained even for designing HOTIs with the same target bandgap width. Some representative nontrivial HOTIs with target bandgap widths of 0.1, 0.2, 0.3 and 0.4 are illustrated in Table 2, and their design variables, the expected and actual output vectors are presented in Appendix C. It can be found that, as the width of the target bandgap gets larger, the diversity of the optimized design becomes weaker and the inclusion phase gets larger.

4.2.2. Optimized HOTI with the largest width of nontrivial bandgap

Using the objective function expressed in Eq. (6), mathematical formulation (5) is solved according to the MTL-enhanced solution procedure illustrated in Fig. 5 again. From 100 random starting points, we obtain an optimized HOTI illustrated by Fig. 7(a) with the design variables $r^* = (0.641, 0.585, 0.554)^\top$. The corresponding expected output vector is $\bar{\omega}_1^* = 1.133$, $\bar{\omega}_2^* = 1.618$ and $\bar{\omega}_2^* - \bar{\omega}_1^* = 0.471$. By modeling the optimized design in COMSOL, the normalized band structure is presented in Fig. 7(b), in which the second and the third bands are close to flat to produce the widest nontrivial bandgap in the design space. The corresponding simulated values are $\hat{\omega}_1^* = 1.131$, $\hat{\omega}_2^* = 1.600$ and $\hat{\omega}_2^* - \hat{\omega}_1^* = 0.468$, with relative errors of 0.12%, 1.12% and 0.64% as compared to the predicted values, respectively. Furthermore, the related symmetry indicators determining the topological properties are listed in Fig. 7(c). As shown by the states of the eigenmodes at the high symmetry points illustrated in Fig. 7(d), the parity of the eigenmode at the X-point is changed in the target bandgap, and this is consistent with the predicted bulk polarization $(\frac{1}{2}, \frac{1}{2})$ exactly.

To further illustrate the topological corner state, a supercell composed of 8×8 optimized unit cells is analyzed in COMSOL as Fig. 8(a). In the eigenfrequency spectrum presented in Fig. 8(c), the blue points illustrate the bulk states, the edge and the corner states are marked as the green and red points. As compared to the band structure of the optimized unit cell in Fig. 7(b), the frequency ranges of the bulk states are consistent with the passing bands, while the edge and corner states appear at the nontrivial topological bandgap, and this is consistent with the nontrivial topological properties. Some of the representative bulk, edge and corner states are illustrated by Fig. 8(d)–(f), respectively.

4.2.3. Validation and application of the optimized HOTIs

Since one of the distinctive features of the 2D HOTIs is the ability to support topological corner states robust to defects, the supercells of three representative HOTIs with normalized bandgap widths of 0.1, 0.25 and 0.468 are analyzed by COMSOL. As shown in Fig. 9, both the perfect supercells and their counterparts with defects (with the geometry models illustrated by Figs. 8(a) and 8(b) respectively) support a corner state. Comparing the zoomed-in images, for those three optimized HOTIs in Fig. 9, as the nontrivial bandgap gets wider, more localized corner states are produced to better concentrate the energy, which would be very beneficial in practical applications. This demonstrates the significance of the proposed optimal design formulation of higher-order topological insulators.

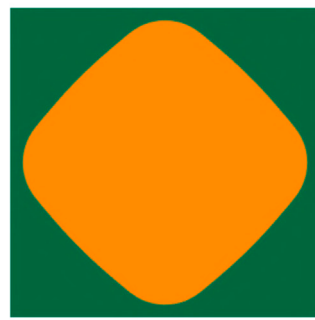
Furthermore, the HOTI with maximized bandgap width (Fig. 7(a)) is used in a programmable high-resolution imaging device illustrated by Fig. 10(a), in which the imaging letters “DUT” written in vacuum

Table 2

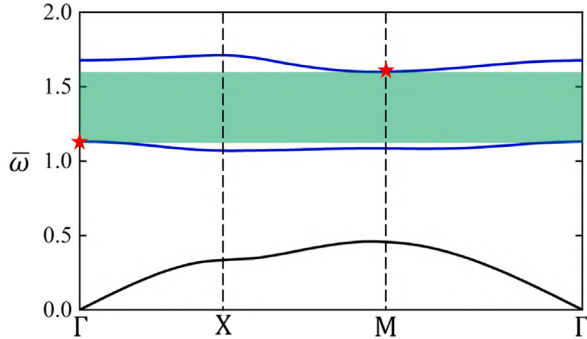
Representative unit cells of mechanical nontrivial HOTIs with specialized normalized bandgap widths of 0.1, 0.2, 0.3 and 0.4, respectively.

Normalized width	1	2	3	4	5	6	7	8
0.1								
0.2								
0.3								
0.4								

(a)



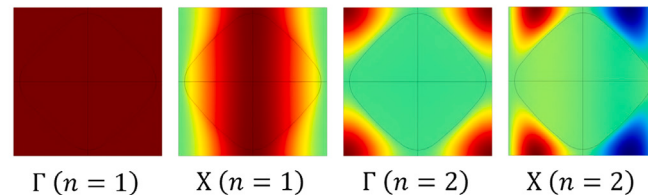
(b)



(c)

C_{4v}	Γ	X
$n = 1$	+1	+1
$n = 2$	+1	-1

(d)

**Fig. 7.** The optimized HOTI with a maximized width of target nontrivial bandgap: (a) the geometry model of the unit cell; (b) normalized band structure of the unit cell; (c) the associated symmetry indicators and (d) the states of the eigenmodes at high symmetry points Γ and X.

are programmed to take the advantages of the topological corner states. On the one hand, the vacuums are topological trivial phases, so corner states exist in the interface of the vacuums and optimal HOTIs; on the other hand, these vacuums also play as defects to the perfect supercell composed of optimal HOTIs, therefore the topology is not destroyed and only a slight frequency shift of the corner states could be observed. Fig. 10(b) shows an expected distribution of displacement intensity through the eigenfrequency simulation, which is excited ($\bar{\omega} = 1.490$, as a shift of its original value of 1.391 in Fig. 8) within the bulk gap and therefore is induced by the topological corner states. Being able to confine most of the energy at the expected corners, the optimized HOTI with highly localized corner states is an excellent building block for topologically functional imaging devices [9].

5. Concluding remarks

The present work develops a machine learning-enhanced fast design paradigm for higher-order topological insulators. The scattering phase

in a C_{4v} -symmetric unit cell is described as Moving Morphable Component with only three design variables. Besides fewer design variables, the modeling, numerical analysis and fabrication could take advantage of the explicit and smooth boundary of the unit cells described by the MMC method as well. This makes the MMC method suitable for the optimal design of topological materials.

Under the explicit topology optimization framework, a mathematical formulation is developed for the rational design of higher-order topological insulators. To solve the bottleneck in the solution process, a multitask learning (MTL) based deep neural network is constructed to simultaneously predict the continuum-valued bounds of the concerned bandgap and the discrete-valued bulk polarization. With the help of the MultiStart solver and the backpropagation algorithm, mechanical HOTIs with highly localized corner states can be obtained by the MTL-assisted solution procedure within 45 s in a desktop workstation,

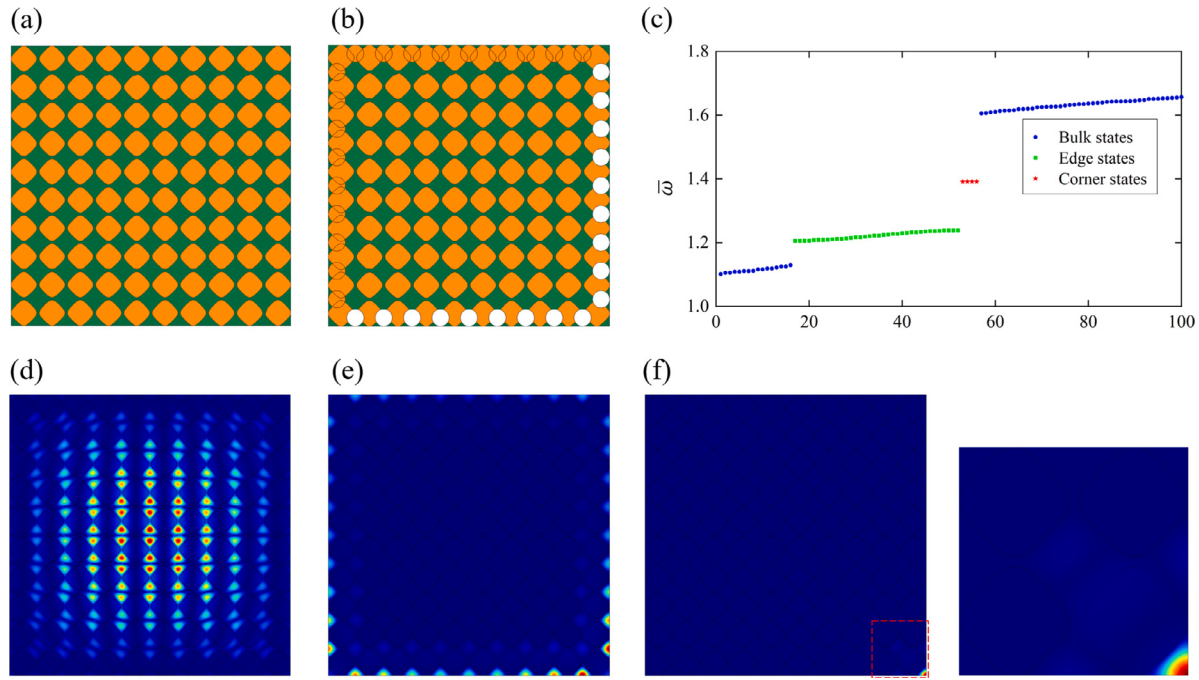


Fig. 8. Simulation results of the supercell composed of 8×8 optimized HOTIs in Fig. 7(a). (a) The geometry model of the perfect supercell; (b) the geometry model of the supercell with defects (the radii of cavities and disorders are all 0.3\AA); (c) the normalized eigenfrequency spectrum of the perfect supercell; (d) the bulk state at the normalized frequency of 1.605 and (e) the edge state at the normalized frequency of 1.239; (f) the corner state at the normalized frequency of 1.391.

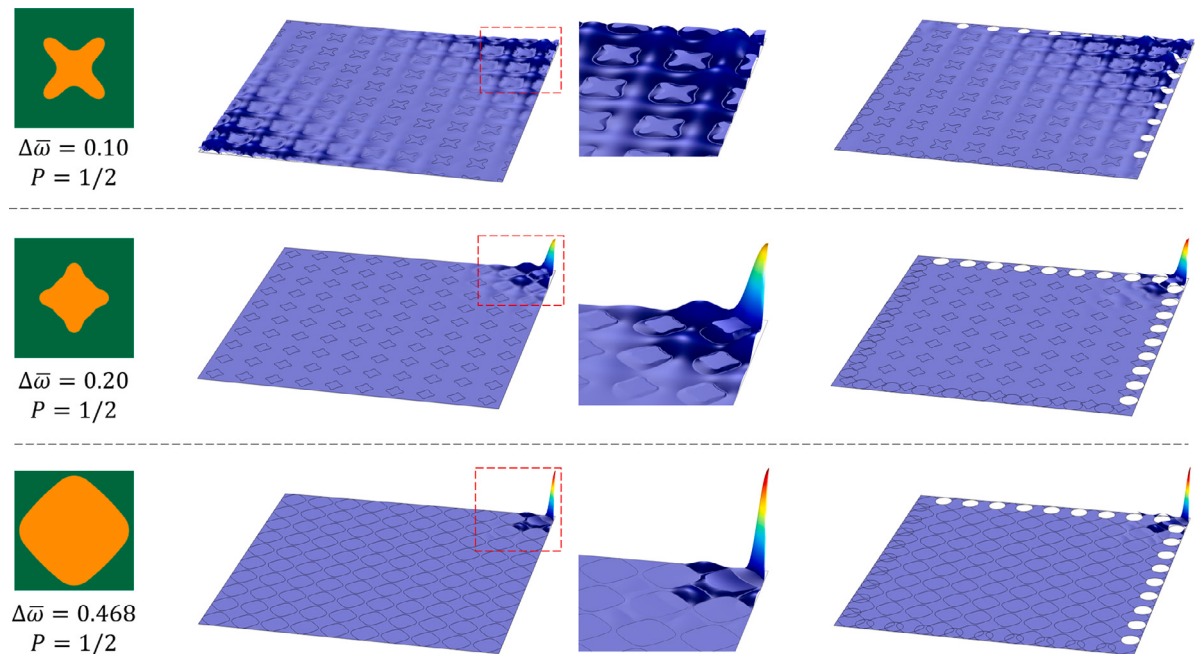


Fig. 9. The topological corner states of the perfect supercells and the supercells with defects composed of HOTIs with normalized bandgap width 0.1, 0.2 and 0.468 (maximized), respectively.

achieving roughly 3–4 orders improvement in efficiency⁵. A novel

⁵ Optimized HOTIs can also be obtained by solving the mathematical formulation (5) and (6) by GA. Setting the GA parameters the same as [44], the solution process converges within about 80–100 generations. Since the population size is 50, and the average time cost for obtaining the output vector is 16.63 s using COMSOL in the same computer, the cost of the classic topology optimization method is about 1478–1848 times of the duration of the proposed ML-enhanced topology optimization approach.

programmable mechanical imaging device demonstrates that optimized HOTIs can be further used as a basic building block of advanced devices.

The present ML-enhanced fast design paradigm can be extended to design topological materials in different physical systems and with different symmetry groups. Furthermore, by collecting the fast design procedures for topological insulators with different symmetries and in different classes together, it is possible to construct a database for phononic and photonic topological materials, which can efficiently output unit cell models from on-demand requirements. This could

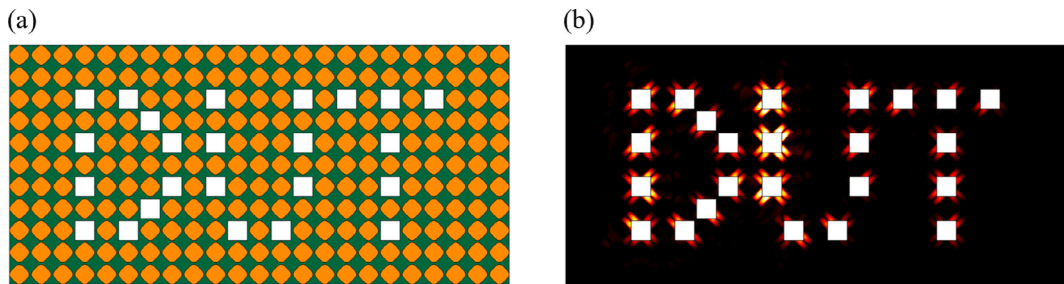


Fig. 10. A novel programmable imaging device composed by the optimized HOTI in Fig. 7(a): (a) the geometry model of the mechanical imaging device; (b) the energy intensity distribution with the excited letters “DUT” induced by topological corner states.

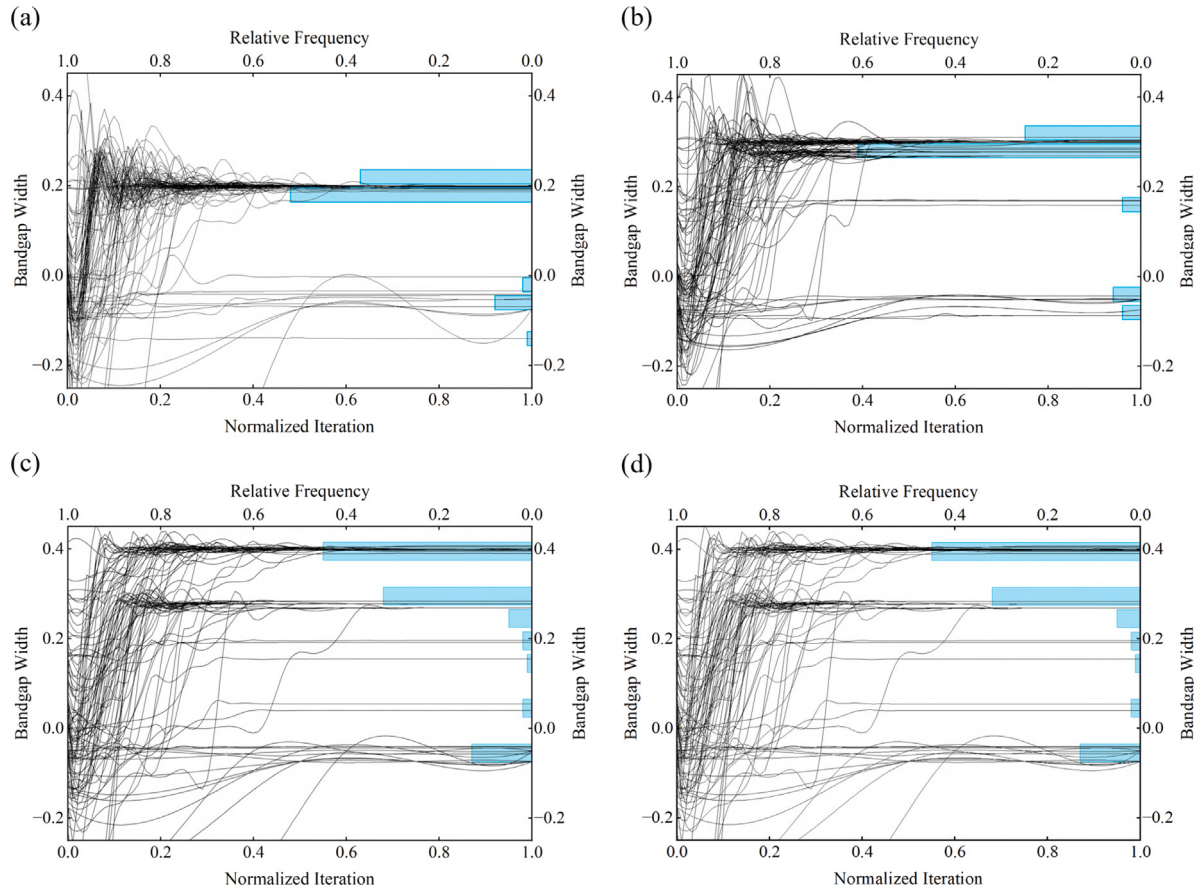


Fig. 11. The iteration histories and the histograms of $\omega_2 - \omega_1$ from 100 random starting points with its specialized values as: (a) 0.2; (b) 0.3; (c) 0.4 and (d) maximum.

be significant for promoting the applications of topological materials. Related study is currently under intensive investigation and will be reported in future works.

CRediT authorship contribution statement

Zongliang Du: Conceptualization, Methodology, Supervision, Formal analysis, Writing – original draft, Writing – review & editing, Funding acquisition. **Jiachen Luo:** Formal analysis, Software, Visualization, Writing – original draft, Writing – review & editing. **Zhiang Xu:** Software, Visualization, Writing – original draft, Writing – review & editing. **Zhenhao Jiang:** Software, Visualization, Review and editing. **Xianggui Ding:** Visualization, Discussion, Writing – review & editing. **Tianchen Cui:** Discussion, Writing – review & editing. **Xu Guo:** Conceptualization, Methodology, Supervision, Writing – review & editing, Funding acquisition.

Declaration of competing interest

The authors declare that they have no known competing financial interests or personal relationships that could have appeared to influence the work reported in this paper.

Data availability

Data will be made available on request.

Acknowledgments

The financial supports from the National Natural Science Foundation, China (11821202, 12002073), the National Key Research and Development Plan, China (2020YFB1709401), Dalian Talent Innovation Program (2020RQ099), the Fundamental Research Funds for the Central Universities, China (DUT20RC(3)020), and 111 Project, China (B14013) are gratefully acknowledged.

Table 3

Comparison of the prediction accuracies of the MTL neural network on the test dataset with different input and output vectors.

	$\bar{\omega}_1$	$\bar{\omega}_2$	Prediction accuracy of T		Absolute errors of bandgap width	
			$Y_2 - Y_1$	Y_3		
$X = (r_1, r_2, r_3)^\top$	1.97%	1.76%	97.55%	0.0179	0.0169	
$Y = (\bar{\omega}_1, \bar{\omega}_2, \bar{\omega}_2 - \bar{\omega}_1, T)^\top$						
$X = (R_1, R_2, \dots, R_{22})^\top$	2.02%	1.62%	97.45%	0.0196	–	
$Y = (\bar{\omega}_1, \bar{\omega}_2, T)^\top$						
$X = (R_1, R_2, \dots, R_{22})^\top$	1.65%	1.37%	98.10%	0.0158	0.0141	
$Y = (\bar{\omega}_1, \bar{\omega}_2, \bar{\omega}_2 - \bar{\omega}_1, T)^\top$						

Table 4Detailed information of the optimized designs in Table 2. The symbols ($\hat{\cdot}$) and ($\hat{\cdot}$) denote the predicted values by the MTL model and simulated values by COMSOL, respectively.

Width	Index	Design variables	$\bar{\omega}_1$	$\bar{\omega}_2$	$\bar{\omega}_2 - \bar{\omega}_1$	T	$\hat{\omega}_1$	$\hat{\omega}_2$	$\hat{\omega}_2 - \hat{\omega}_1$	\hat{T}
0.1	1	(0.378, 0.207, 0.042) $^\top$	0.814	0.914	0.100	1	0.812	0.913	0.101	1
	2	(0.011, 0.516, 0.453) $^\top$	0.945	1.045	0.100	1	0.951	1.051	0.101	1
	3	(0.143, 0.264, 0.308) $^\top$	0.761	0.861	0.100	1	0.753	0.854	0.101	1
	4	(0.692, 0.451, 0.382) $^\top$	1.263	1.363	0.100	1	1.258	1.358	0.100	1
	5	(0.498, 0.392, 0.640) $^\top$	1.377	1.477	0.100	1	1.369	1.469	0.100	1
	6	(0.558, 0.834, 0.028) $^\top$	1.095	1.195	0.100	1	1.091	1.192	0.100	1
	7	(0.264, 0.987, 0.023) $^\top$	1.136	1.236	0.100	1	1.132	1.230	0.099	1
	8	(0.011, 0.356, 0.431) $^\top$	0.850	0.950	0.100	1	0.864	0.963	0.098	1
0.2	1	(0.494, 0.152, 0.179) $^\top$	0.878	1.078	0.200	1	0.877	1.076	0.199	1
	2	(0.383, 0.348, 0.452) $^\top$	0.878	1.078	0.200	1	0.874	1.073	0.199	1
	3	(0.346, 0.395, 0.320) $^\top$	0.813	1.013	0.200	1	0.800	1.002	0.202	1
	4	(0.539, 0.200, 0.098) $^\top$	0.899	1.099	0.200	1	0.895	1.097	0.202	1
	5	(0.402, 0.233, 0.379) $^\top$	0.835	1.035	0.200	1	0.834	1.035	0.201	1
	6	(0.272, 0.504, 0.213) $^\top$	0.920	1.120	0.200	1	0.899	1.099	0.200	1
	7	(0.558, 0.435, 0.043) $^\top$	0.915	1.115	0.200	1	0.918	1.117	0.199	1
	8	(0.399, 0.288, 0.446) $^\top$	0.891	1.091	0.200	1	0.884	1.084	0.200	1
0.3	1	(0.674, 0.700, 0.444) $^\top$	1.198	1.498	0.300	1	1.191	1.494	0.303	1
	2	(0.384, 0.519, 0.378) $^\top$	0.955	1.255	0.300	1	0.947	1.248	0.301	1
	3	(0.486, 0.360, 0.397) $^\top$	0.879	1.179	0.300	1	0.871	1.170	0.299	1
	4	(0.959, 0.497, 0.686) $^\top$	1.216	1.516	0.300	1	1.235	1.536	0.302	1
	5	(0.595, 0.448, 0.171) $^\top$	0.922	1.222	0.300	1	0.935	1.233	0.298	1
	6	(0.278, 0.624, 0.309) $^\top$	1.080	1.380	0.300	1	1.083	1.384	0.302	1
0.4	1	(0.397, 0.635, 0.487) $^\top$	1.155	1.555	0.400	1	1.149	1.546	0.397	1
	2	(0.465, 0.587, 0.552) $^\top$	1.138	1.538	0.400	1	1.135	1.536	0.400	1
	3	(0.647, 0.674, 0.567) $^\top$	1.238	1.638	0.400	1	1.238	1.637	0.399	1
	4	(0.611, 0.367, 0.485) $^\top$	0.998	1.398	0.400	1	0.997	1.396	0.399	1
	5	(0.654, 0.629, 0.406) $^\top$	1.101	1.501	0.400	1	1.094	1.494	0.400	1

Appendix A. Comparison of the prediction accuracy with different choices of input and output

Although the C_{4v} -symmetric unit cells in Fig. 1(a) can be determined by the three control points based on the B-spline interpolation [34,44], only using the radii of the three control points as input vector may not supply sufficient information to train an accurate machine learning model. It is a natural choice to include more information as input. Alternatively using the images [73], we use the radii of 22 refined interpolation points as the adopted input vector.

On the other hand, the MTL is an approach to inductive transfer by using information from related tasks as an inductive bias, which could improve the learning efficiency, prediction accuracy, and generalization ability of neural networks [68]. Since different tasks have different noise patterns, by averaging over noise patterns, an MTL model's attention can be focused on those features that actually matter to learn a more general representation, and the risk of over-fitting can also be reduced [74]. Based on those facts, the width of the normalized bandgap (i.e., $\bar{\omega}_2 - \bar{\omega}_1$) is added as the third output variable.

The prediction accuracy with different choices of the input and output are presented in Table 3. It is obvious that, the finally adopted input and output vectors have the highest accuracy. Actually, this minor improvement in the accuracy of the prediction model would be very beneficial for obtaining optimized HOTIs with target properties.

Appendix B. The effectiveness of the adoption of the MultiStart solver

Compared to the gradient-free algorithms, the gradient-based algorithm has the advantage of the efficiency of the solution process; nevertheless, it is more likely to be trapped into local optima. Actually, such a situation is more pronounced due to the inevitable errors of the MTL model, and the convergence condition can be met even if the target bandgap width is not achieved.

From 100 random starting points, Fig. 11 plots the iteration histories and the histograms of the normalized bandgap width with different targets, respectively. It can be found that, some of the final solutions do not converge to their desired values.

Appendix C. Detailed information of the optimized designs with specialized bandgap widths

The design variables, the corresponding expected and actual lower bounds, upper bounds, bandgap width and topological labels of the optimized designs in Table 2 are listed in the Table 4. It is obvious that, all the obtained designs are nontrivial higher-order topological insulators. The expected widths of normalized bandgap are all quite close to their exact values. This demonstrates again the effectiveness of the proposed MTL-enhanced fast design framework for higher-order topological insulators.

References

- [1] Hasan M Zahid, Kane Charles Lewis. Colloquium: Topological insulators. *Rev Modern Phys* 2010;82(4):3045–67.
- [2] Qi Xiaoliang, Zhang Shou-Cheng. Topological insulators and superconductors. *Rev Modern Phys* 2011;83(4):1057–110.
- [3] Benalcazar Wladimir A, Bernevig B Andrei, Hughes Taylor L. Quantized electric multipole insulators. *Science* 2017;357(6346):61–6.
- [4] Schindler Frank, Cook Ashley M, Vergniory Maia G, Wang Zhijun, Parkin Stuart SP, Bernevig B Andrei, et al. Higher-order topological insulators. *Sci Adv* 2018;4(6):eaat0346.
- [5] Xue Haoran, Yang Yahui, Gao Fei, Chong Yidong, Zhang Baile. Acoustic higher-order topological insulator on a kagome lattice. *Nature Mater* 2019;18(2):108–12.
- [6] Ni Xiang, Weiner Matthew, Alu Andrea, Khanikaev Alexander B. Observation of higher-order topological acoustic states protected by generalized chiral symmetry. *Nature Mater* 2019;18(2):113–20.
- [7] Noh Jijo, Benalcazar Wladimir A, Huang Sheng, Collins Matthew J, Chen Kevin P, Hughes Taylor L, et al. Topological protection of photonic mid-gap defect modes. *Nat Photonics* 2018;12(7):408–15.
- [8] Mittal Sunil, Orre Venkata Vikram, Zhu Guanyu, Gorlach Maxim A, Podubny Alexander, Hafezi Mohammad. Photonic quadrupole topological phases. *Nat Photonics* 2019;13(10):692–6.
- [9] Zhang Zhiwang, Long Houyou, Liu Chen, Shao Chen, Cheng Ying, Liu Xiaojun, et al. Deep-subwavelength holey acoustic second-order topological insulators. *Adv Mater* 2019;31(49):1904682.
- [10] Zhang Zhiwang, López María Rosendo, Cheng Ying, Liu Xiaojun, Christensen Johan. Non-Hermitian sonic second-order topological insulator. *Phys Rev Lett* 2019;122(19):195501.
- [11] Xie Bi-Ye, Su Guang-Xu, Wang Hong-Fei, Su Hai, Shen Xiao-Peng, Zhan Peng, et al. Visualization of higher-order topological insulating phases in two-dimensional dielectric photonic crystals. *Phys Rev Lett* 2019;122(23):233903.
- [12] El Hassan Ashraf, Kunst Flore K, Moritz Alexander, Andler Guillermo, Bergholtz Emil J, Bourennane Mohamed. Corner states of light in photonic waveguides. *Nat Photonics* 2019;13(10):697–700.
- [13] Wu Qian, Chen Hui, Li Xiaopeng, Huang Guoliang. In-plane second-order topologically protected states in elastic kagome lattices. *Phys Rev Appl* 2020;14(1):014084.
- [14] Fan Haiyan, Xia Baizhan, Tong Liang, Zheng Shengjie, Yu Dejie. Elastic higher-order topological insulator with topologically protected corner states. *Phys Rev Lett* 2019;122(20):204301.
- [15] Zhang Li, Yang Yihao, Lin Zhi-Kang, Qin Pengfei, Chen Qiaolu, Gao Fei, et al. Higher-order topological states in surface-wave photonic crystals. *Adv Sci* 2020;7(6):1902724.
- [16] Kim Kwang-Hyon, Om Kwang-Kwon. Multiband photonic topological valley-Hall edge modes and second-order corner states in square lattices. *Adv Opt Mater* 2021;9(8):2001865.
- [17] Xue Haoran, Yang Yahui, Liu Guigeng, Gao Fei, Chong Yidong, Zhang Baile. Realization of an acoustic third-order topological insulator. *Phys Rev Lett* 2019;122(24):244301.
- [18] Yang Linyun, Wu Ying, Yu Kaiping, Zhao Rui, Wang Wei, Bonello Bernard, Djafari-Rouhani Bahram. Robust Fano resonance between mechanical first-and second-order topological states. *Int J Mech Sci* 2022;236:107768.
- [19] Duan Guiju, Zheng Shengjie, Lin Zhi-Kang, Jiao Junrui, Liu Jianting, Jiang Zihan, et al. Numerical and experimental investigation of second-order mechanical topological insulators. *J Mech Phys Solids* 2023;174:105251.
- [20] Pal Raj Kumar, Ruzzene Massimo. Edge waves in plates with resonators: an elastic analogue of the quantum valley Hall effect. *New J Phys* 2017;19(2):025001.
- [21] Chen Hui, Nassar Hussein, Huang Guoliang. A study of topological effects in 1D and 2D mechanical lattices. *J Mech Phys Solids* 2018;117:22–36.
- [22] Chen Hui, Nassar Hussein, Norris Andrew N, Hu Gengkai, Huang Guoliang. Elastic quantum spin Hall effect in kagome lattices. *Phys Rev B* 2018;98(9):094302.
- [23] Chen Yi, Liu Xiaoning, Hu Gengkai. Topological phase transition in mechanical honeycomb lattice. *J Mech Phys Solids* 2019;122:54–68.
- [24] Zhou Weijian, Lim CW. Topological edge modeling and localization of protected interface modes in 1D phononic crystals for longitudinal and bending elastic waves. *Int J Mech Sci* 2019;159:359–72.
- [25] Zhou Weijian, Wu Bin, Chen Zhenyu, Chen Weiqiu, Lim CW, Reddy JN. Actively controllable topological phase transition in homogeneous piezoelectric rod system. *J Mech Phys Solids* 2020;137:103824.
- [26] Chen Yingjie, Wu Bin, Li Jian, Rudykh Stephan, Chen Weiqiu. Low-frequency tunable topological interface states in soft phononic crystal cylinders. *Int J Mech Sci* 2021;191:106098.
- [27] Ma Tian-Xue, Fan Quan-Shui, Zhang Chuanzeng, Wang Yue-Sheng. Flexural wave energy harvesting by the topological interface state of a phononic crystal beam. *Extreme Mech Lett* 2022;50:101578.
- [28] Christiansen Rasmus E, Wang Fengwen, Sigmund Ole. Topological insulators by topology optimization. *Phys Rev Lett* 2019;122(23):234502.
- [29] Christiansen Rasmus E, Wang Fengwen, Sigmund Ole, Stobbe Søren. Designing photonic topological insulators with quantum-spin-Hall edge states using topology optimization. *Nanophotonics* 2019;8(8):1363–9.
- [30] Nanthakumar SS, Zhuang Xiaoying, Park Harold S, Nguyen Chuong, Chen Yanyu, Rabczuk Timon. Inverse design of quantum spin Hall-based phononic topological insulators. *J Mech Phys Solids* 2019;125:550–71.
- [31] Chen Yafeng, Meng Fei, Jia Baohua, Li Guangyao, Huang Xiaodong. Inverse design of photonic topological insulators with extra-wide bandgaps. *Phys Status Solidi (RRL)-Rapid Res Lett* 2019;13(9):1900175.
- [32] Dong Hao-Wen, Zhao Sheng-Dong, Zhu Rui, Wang Yue-Sheng, Cheng Li, Zhang Chuanzeng. Customizing acoustic Dirac cones and topological insulators in square lattices by topology optimization. *J Sound Vib* 2020;493:115687.
- [33] Lu Yan, Park Harold S. Double Dirac cones and topologically nontrivial phonons for continuous square symmetric $C_{4(v)}$ and $C_{2(v)}$ unit cells. *Phys Rev B* 2021;103(6):064308.
- [34] Du Zongliang, Chen Hui, Huang Guoliang. Optimal quantum valley Hall insulators by rationally engineering Berry curvature and band structure. *J Mech Phys Solids* 2020;135:103784.
- [35] Yang Jishi, Liu Yaolu, Sun Dongyang, Hu Ning, Ning Huiming. Inverse design of valley-like edge states of sound degenerated away from the high-symmetry points in a square lattice. *Materials* 2022;15(19):6697.
- [36] Zhang Jinhao, Wang Fengwen, Sigmund Ole, Gao Liang, Christiansen Rasmus E. Ultra-broadband edge-state pair for zigzag-interfaced valley Hall insulators. *Sci China Phys Mech Astron* 2022;65(5):257011.
- [37] Luo Jiachen, Du Zongliang, Liu Chang, Mei Yue, Zhang Weisheng, Guo Xu. Moving morphable components-based inverse design formulation for quantum valley/spin Hall insulators. *Extreme Mech Lett* 2021;45:101276.
- [38] Chen Yafeng, Meng Fei, Kivshar Yuri, Jia Baohua, Huang Xiaodong. Inverse design of higher-order photonic topological insulators. *Phys Rev Res* 2020;2(2):023115.
- [39] Chen Yafeng, Li Jensen, Zhu Jie. Topology optimization of quantum spin Hall effect-based second-order phononic topological insulator. *Mech Syst Signal Process* 2022;164:108243.
- [40] Chen Yafeng. On the use of topology optimized band gap structures for the realization of second-order acoustic topological insulators with valley-selective corner states. *Struct Multidiscip Optim* 2022;65(4):115.
- [41] Chen Yafeng, Lan Zhihao, Zhu Jie. Inversely designed second-order photonic topological insulator with multiband corner states. *Phys Rev Appl* 2022;17(5):054003.
- [42] Zheng Zhoufu, Yin Jianfei, Wen Jihong, Yu Dianlong, Chen Xun. Switchable corner states in phononic crystals realized by inverse design. *Int J Mech Sci* 2023;243:108035.
- [43] Chen Yafeng, Lan Zhihao, Su Zhongqing, Zhu Jie. Inverse design of photonic and phononic topological insulators: a review. *Nanophotonics* 2022;11(19):4347–62.
- [44] Luo Jiachen, Du Zongliang, Guo Yilin, Liu Chang, Zhang Weisheng, Guo Xu. Multi-class, multi-functional design of photonic topological insulators by rational symmetry-indicators engineering. *Nanophotonics* 2021;10(18):4523–31.
- [45] Long Yang, Ren Jie, Li Yunhui, Chen Hong. Inverse design of photonic topological state via machine learning. *Appl Phys Lett* 2019;114(18):181105.
- [46] Long Yang, Ren Jie, Chen Hong. Unsupervised manifold clustering of topological phononics. *Phys Rev Lett* 2020;124(18):185501.
- [47] Araki Hiromu, Mizoguchi Tomonari, Hatsugai Yasuhiro. Phase diagram of a disordered higher-order topological insulator: A machine learning study. *Phys Rev B* 2019;99(8):085406.
- [48] Wu Bei, Ding Kun, Chan Che Ting, Chen Yuntian. Machine prediction of topological transitions in photonic crystals. *Phys Rev Appl* 2020;14(4):044032.
- [49] Molignini Paolo, Zegarra Antonio, van Nieuwenburg Everard, Chitra Ramasubramanian, Chen Wei. A supervised learning algorithm for interacting topological insulators based on local curvature. *SciPost Phys* 2021;11(3):073.
- [50] He Liangshu, Wen Zhihui, Jin Yabin, Torrent Daniel, Zhuang Xiaoying, Rabczuk Timon. Inverse design of topological metaplates for flexural waves with machine learning. *Mater Des* 2021;199:109390.
- [51] He Liangshu, Guo Hongwei, Jin Yabin, Zhuang Xiaoying, Rabczuk Timon, Li Yan. Machine-learning-driven on-demand design of phononic beams. *Sci China Phys Mech Astron* 2022;65:214612.
- [52] Jin Yabin, He Liangshu, Wen Zhihui, Mortazavi Bohayra, Guo Hongwei, Torrent Daniel, et al. Intelligent on-demand design of phononic metamaterials. *Nanophotonics* 2022;11(3):439–60.
- [53] Du Zongliang, Ding Xianggui, Chen Hui, Liu Chang, Zhang Weisheng, Luo Jiachen, et al. Optimal design of topological waveguides by machine learning. *Front Mater* 2022;9:1075073.
- [54] Sigmund Ole, Maute Kurt. Topology optimization approaches: A comparative review. *Struct Multidiscip Optim* 2013;48(6):1031–55.
- [55] Guo Xu, Zhang Weisheng, Zhong Wenliang. Doing topology optimization explicitly and geometrically—a new moving morphable components based framework. *J Appl Mech* 2014;81(8):081009.
- [56] Zhang Weisheng, Yuan Jie, Zhang Jian, Guo Xu. A new topology optimization approach based on Moving Morphable Components (MMC) and the ersatz material model. *Struct Multidiscip Optim* 2016;53:1243–60.

- [57] Zhang Weisheng, Yang Wanying, Zhou Jianhua, Li Dong, Guo Xu. Structural topology optimization through explicit boundary evolution. *J Appl Mech* 2017;84(1):011011.
- [58] Du Zongliang, Cui Tianchen, Liu Chang, Zhang Weisheng, Guo Yilin, Guo Xu. An efficient and easy-to-extend Matlab code of the Moving Morphable Component (MMC) method for three-dimensional topology optimization. *Struct Multidiscip Optim* 2022;65:158.
- [59] Fu Liang. Topological crystalline insulators. *Phys Rev Lett* 2011;106(10):106802.
- [60] Fang Chen, Gilbert Matthew J, Bernevig B Andrei. Bulk topological invariants in noninteracting point group symmetric insulators. *Phys Rev B* 2012;86(11):115112.
- [61] Benalcazar Wladimir A, Li Tianhe, Hughes Taylor L. Quantization of fractional corner charge in Cn-symmetric higher-order topological crystalline insulators. *Phys Rev B* 2019;99(24):245151.
- [62] Bradlyn Barry, Elcoro Luis, Cano Jennifer, Vergniory Maia G, Wang Zijun, Felser Claudia, et al. Topological quantum chemistry. *Nature* 2017;547(7663):298–305.
- [63] Po Hoi Chun, Vishwanath Ashvin, Watanabe Haruki. Symmetry-based indicators of band topology in the 230 space groups. *Nature Commun* 2017;8(1):1–9.
- [64] Watanabe Haruki, Po Hoi Chun, Vishwanath Ashvin. Structure and topology of band structures in the 1651 magnetic space groups. *Sci Adv* 2018;4(8):eaat8685.
- [65] Tang Feng, Po Hoi Chun, Vishwanath Ashvin, Wan Xiangang. Comprehensive search for topological materials using symmetry indicators. *Nature* 2019;566(7745):486–9.
- [66] Tang Feng, Po Hoi Chun, Vishwanath Ashvin, Wan Xiangang. Efficient topological materials discovery using symmetry indicators. *Nat Phys* 2019;15(5):470–6.
- [67] Caruana Rich. Multitask learning: A knowledge-based source of inductive bias. In: Proceedings of the tenth international conference on machine learning. Citeseer; 1993, p. 41–8.
- [68] Caruana Rich. Multitask learning. *Mach Learn* 1997;28(1):41–75.
- [69] Kendall Alex, Gal Yarin, Cipolla Roberto. Multi-task learning using uncertainty to weigh losses for scene geometry and semantics. In: Proceedings of the IEEE conference on computer vision and pattern recognition. 2018, p. 7482–91.
- [70] Ioffe Sergey, Szegedy Christian. Batch normalization: Accelerating deep network training by reducing internal covariate shift. In: International conference on machine learning. PMLR; 2015, p. 448–56.
- [71] Srivastava Nitish, Hinton Geoffrey, Krizhevsky Alex, Sutskever Ilya, Salakhutdinov Ruslan. Dropout: a simple way to prevent neural networks from overfitting. *J Mach Learn Res* 2014;15(1):1929–58.
- [72] Loschilov Ilya, Hutter Frank. Decoupled weight decay regularization. 2017, <http://dx.doi.org/10.48550/arXiv.1711.05101>, arXiv e-prints arXiv:1711.05101.
- [73] Li Xiang, Ning Shaowu, Liu Zhanli, Yan Ziming, Luo Chengcheng, Zhuang Zhuo. Designing phononic crystal with anticipated band gap through a deep learning based data-driven method. *Comput Methods Appl Mech Engrg* 2020;361:112737.
- [74] Ruder Sebastian. An overview of multi-task learning in deep neural networks. 2017, arXiv preprint arXiv:1706.05098.